



UvA-DARE (Digital Academic Repository)

Glow with the flow: Quantifying blood flow and photoluminescence signal in biological tissue

Nadort, A.

Publication date

2015

Document Version

Final published version

[Link to publication](#)

Citation for published version (APA):

Nadort, A. (2015). *Glow with the flow: Quantifying blood flow and photoluminescence signal in biological tissue*. [Thesis, fully internal, Universiteit van Amsterdam].

General rights

It is not permitted to download or to forward/distribute the text or part of it without the consent of the author(s) and/or copyright holder(s), other than for strictly personal, individual use, unless the work is under an open content license (like Creative Commons).

Disclaimer/Complaints regulations

If you believe that digital publication of certain material infringes any of your rights or (privacy) interests, please let the Library know, stating your reasons. In case of a legitimate complaint, the Library will make the material inaccessible and/or remove it from the website. Please Ask the Library: <https://uba.uva.nl/en/contact>, or a letter to: Library of the University of Amsterdam, Secretariat, P.O. Box 19185, 1000 GD Amsterdam, The Netherlands. You will be contacted as soon as possible.



6

QUANTITATIVE IMAGING OF SINGLE UPCONVERSION
NANOPARTICLES IN BIOLOGICAL TISSUE

Adapted from:

A. Nadort, V. K. Sreenivasan, Z. Song, E. A. Grebenik, A. V. Nechaev, V. A. Semchishen, V. Y. Panchenko, and A. V. Zvyagin, "Quantitative imaging of single upconversion nanoparticles in biological tissue," *PLoS One* 8, e63292 (2013).

6

ABSTRACT The unique luminescent properties of new-generation synthetic nanomaterials, upconversion nanoparticles (UCNPs), enable high-contrast optical biomedical imaging by suppressing the background of biological tissue autofluorescence and evading high tissue absorption. This raised high expectations on the UCNP utilities for intracellular and deep tissue imaging, such as whole animal imaging. At the same time, the critical nonlinear dependence of the UCNP luminescence on the excitation intensity results in dramatic signal reduction at (~ 1 cm) depth in biological tissue. Here, we report on the experimental and theoretical investigation of this trade-off aiming at the identification of optimal application niches of UCNPs e.g. biological liquids and subsurface tissue layers. As an example of such applications, we report on single UCNP imaging through a layer of haemolysed blood. To extend this result towards *in vivo* applications, we quantified the optical properties of single UCNPs and theoretically analyzed the prospects of single-particle detectability in scattering and absorbing bio-tissue using a human skin model. The model predicts that a single 70-nm UCNP would be detectable at skin depths up to 400 μm , unlike a hardly detectable single fluorescent (fluorescein) dye molecule. UCNP-assisted imaging in the ballistic regime thus allows for excellent applications niches, where high sensitivity is the key requirement.

6.1 INTRODUCTION

Optical imaging of biological tissues provides highly informative, non-invasive and inexpensive means to assess the tissue physiological status and functionality, especially for diagnosis of pathological sites. Labelling these tissue sites with luminescent biocomplexes, often referred to as molecular probes, improves localization accuracy and sensitivity. Deployment of a new class of molecular probes whose excitation/emission falls into the so-called biological tissue transparency window (650 nm – 1300 nm), allows deeper imaging in virtue of the minimized absorption and scattering of biological tissue in this near-infrared (NIR) wavelength range [1, 2]. For example, specific labelling of cancerous lesions with a molecular probe based on indocyanine green (the only NIR organic dye approved for routine clinical procedures) provided up to a 4-fold increase in the tumour imaging contrast in comparison with that achieved using the intrinsic haemoglobin spectral signature and tissue scattering [3, 4].

The development of NIR-emitting probes is traditionally directed towards organic dyes, but more recent studies have demonstrated considerable promise of inorganic nanoparticle-based probes, such as quantum dots (QDs) and most novel upconversion nanoparticles (UCNPs) [5, 6]. Organic NIR-dyes are favourably small, easily dispersed in an aqueous environment and can be functionalized using established bioconjugation protocols. However, their poor thermal and photochemical stability (photobleaching) and a low fluorescence quantum yield (QY) (5-25% in NIR, with propensity to deteriorate in biological environments) are inferior in comparison with QDs whose attractive optical properties include size-tunable optical absorption and emission, high photochemical stability and high QY (20-70% in NIR), in addition to high thermal stability [7]. On the other hand, QD fluorescence is intermittent ('blinking') hindering applications such as single molecule tracking, while QD intrinsic toxicity largely precludes their use *in vivo* [8]. UCNPs share the high photochemical and thermal stability of QDs and other inorganic nanomaterials, complemented with non-blinking emission and demonstrated biocompatibility. In addition, UCNPs can be employed as a docking platform for high drug payloads for targeted delivery [9]. The key advantage of UCNPs is their unique photochemical structure that enables "upconversion" of NIR excitation light (980 nm) of modest intensity (100 W/cm²) to the higher energy visible emission (450 - 850 nm) [10]. Since no known biological molecule is capable of such conversion [1, 11], the intrinsic tissue fluorescence, termed autofluorescence, can be eliminated in the detection path by conventional optical short-pass filtering. In addition, the exceptionally long (sub-milliseconds) luminescence lifetimes of UCNPs allow realization of time-gated detection schemes that can completely suppress the residual back-scattered excitation light bleeding through the (interference) spectral filters [12]. Since *in vivo* imaging performance is crucially dependent on the contrast provided by the molecular probe [1], background-free detection of UCNPs is very promising, as has been shown by the autofluorescence-free trans-illumination imaging in mice using biocompatible UCNPs [13, 14].

The unique upconversion property of UCNPs is a result of the sequential photon absorption and energy transfer processes within an inorganic host matrix, where hexagonal phase β -NaYF₄ co-doped with trivalent lanthanide ions reported to be the most efficient [15, 16]. These dopant ions are classified as sensitizers and activators considering their respective

roles in the UCNP absorption and emission. The sensitizer, typically Ytterbium ion (Yb^{3+}), absorbs the NIR-radiation energy and transfers it non-radiatively to the closely spaced neighbouring Yb^{3+} , forming a network of excited Yb^{3+} (referred to as delocalized quasi-exciton [17]) until the energy is seized by activator ions, usually Erbium (Er^{3+}), or Thulium (Tm^{3+}). The activator makes a transition to a metastable excited state, from where it can coalesce with a nearby excited Yb^{3+} -ion and transfer to the next energy level (a process called energy transfer upconversion) at the expense of the participating Yb^{3+} decaying to the ground state. Multiple-step energy transfer upconversion is also possible. The activator can return to the ground state by radiating a photon in the visible or NIR wavelength range. The upconversion emission results from the absorption of 2 or more NIR photons, and hence is supralinear versus the excitation intensity, I_{ex} , as quantified by the conversion efficiency (η_{uc}) addressed in Section 6.2.2. In contrast with other anti-Stokes processes occurring at $I_{\text{ex}} \sim \times 10^5 \text{ W/cm}^2$ [18] the energy transfer upconversion occurs via real metastable excited state(s) at rather modest $I_{\text{ex}} \sim 1 \times 10^2 \text{ W/cm}^2$ that is readily achievable by focusing a continuous-wave excitation beam.

The specific photophysical properties of upconversion nanoparticles entail several challenges for optical biomedical imaging. Firstly, the quasi-excitonic nature of UCNP excitation renders the emission size dependent and susceptible to surface quenching [19] and (biological) environment, which causes reduction of η_{uc} values that are generally small compared to these of QDs or organic fluorescent dyes. Values of η_{uc} are typically around 1% for nanoparticle diameters of $\sim 50 \text{ nm}$, shown to be the optimal size for cellular receptor-mediated internalization [20]. Secondly, η_{uc} is dependent on the excitation intensity and increases to a plateau value, for which the I_{ex} is referred to as saturation intensity, I_{sat} ($I_{\text{sat}} \cong 1 \times 10^2 \text{ W/cm}^2$). Keeping I_{ex} close to I_{sat} is preferable for biomedical imaging.

This dependency of η_{uc} on I_{ex} poses the main challenge for UCNP-assisted optical imaging in deep (live) tissue layers exceeding centimetre(s). Indeed, the realization of I_{sat} by focusing is hardly possible in turbid biotissue, while the laser power is limited by the allowed maximum permissible exposures (MPEs). The UCNP luminescence signal is therefore diminished with depth as was demonstrated in tissue phantom experiments [14]. In another recent study, the critical dependence of η_{uc} versus depth was manifested by the considerable deterioration of axial and lateral resolution of full-field upconversion microscopy at depths of $\sim 300\text{-}400 \mu\text{m}$ [21]. These results urge identification of practical application niches for UCNPs that will benefit from the aforementioned advantages of UCNPs, while not being restricted by their limitations. Promising scenarios include imaging in biological fluids, thick slices and subsurface tissue layers, where the UCNP-based molecular probe contrast is expected to be superior to that of existing molecular probes, including organic fluorescent dyes.

This work aims to explore the cutting-edge optical imaging scenario represented by a single UCNP buried in an absorbing biological environment, which was demonstrated by single-UCNP imaging through a layer of haemolysed blood. We believe this result has not been reported before [22-25]. We report on absolute conversion efficiency and spectral properties of single UCNPs. The subsequent thorough characterization of the UCNP emission signal and excitation/detection parameters allowed projection of the experimental

results onto a theoretical model, generalized to biomedical imaging applications of extreme sensitivity in challenging *in vivo* environments. Single-UCNP imaging was modelled to be feasible in skin depths of a few hundred micrometers, with superior contrast compared to a conventional fluorescent dye molecule. The results show that imaging in the ballistic regime allows for excellent applications of UCNP-guided imaging in life sciences where high sensitivity is a key requirement.

6.2 MATERIALS AND METHODS

6.2.1 Synthesis

Synthesis reagents

Y_2O_3 , Yb_2O_3 , Er_2O_3 , sodium trifluoroacetate 99%, trifluoroacetic acid 98%, oleic acid 90%, 1-octadecene 90% (all purchased from Sigma-Aldrich).

Synthesis protocol of β -NaYF₄

Yb,Er nanophosphors: The mixture of Y_2O_3 (0.78 mmol), Yb_2O_3 (0.20 mmol), Er_2O_3 (0.02 mmol) was suspended in 70% trifluoroacetic acid (20 ml) and gently refluxed until a clear solution was obtained (\approx 6 h), then cooled to room temperature. After the solution was evaporated, the formed residue was dried in vacuum (0.1 torr, 3h). The resulting slurry was thoroughly grinded in agate mortar into a fine homogenous powder. This rare-earth trifluoroacetate mixture and sodium trifluoroacetate (1 mmol) were added to oleic acid (6 ml) and 1-octadecene (6 ml) in a three-neck flask, with a thermometer, septum stopper and glass magnetic stirrer. The solution was heated to 100 °C and stirred under vacuum for 30 min for degassing and removal of water. The mixture was subsequently gradually heated at a rate of 8 °C/min to 290 °C, and kept at this temperature for 45 min under argon atmosphere. A solution of sodium trifluoroacetate (1 mmol) in oleic acid (2 ml) and 1-octadecene (2 ml), heated to 85°C, was added to the reaction, after which the reaction temperature was raised to 330°C and stirred for 15 min under argon. Next, isopropanol (130 ml) was added to the cooled solution and the mixture was centrifuged at 6000 rpm for 30 min. The resultant nanoparticles were washed with absolute ethanol (4 times), dried, dissolved in chloroform (10 ml), precipitated with isopropanol (50 ml) and centrifuged at 4000 rpm for 10 min. The last procedure was repeated 2 times. The residue was dried at room temperature.

6.2.2 Imaging

Transmission electron microscopy

The UCNPs were dissolved in hexane, drop-casted on Formav[®]-coated TEM grids and dried in a desiccator at room temperature. The grids were imaged with a Philips CM10 TEM and analysed using ImageJ free-ware to obtain the UCNP size distributions. For single-UCNP imaging, the hexane solutions were diluted and drop-casted on Formav[®]-coated TEM nickel finder grids for easy navigation. The thinly coated finder grids can be imaged using TEM and optical epi-luminescence systems. In order to find single nanoparticles, low-magnification TEM imaging was carried out gradually zooming into areas of interest to track the UCNP location precisely.

Laser-illuminated inverted epi-luminescence microscope

A wide-field inverted epi-luminescence microscope (Olympus IX70) equipped with a water-immersion objective (40 \times , NA 1.15, Olympus) was modified to allow external laser illumination at the sample plane (fibre-coupled diode laser at wavelength 978 nm, LD980-01CW CXCH-Photonics). In order to achieve uniform illumination of the size-controllable field-of-view at the sample plane, a modified Köhler illumination scheme was designed and built in-house, as shown in Fig. 6.1, with detailed description and ray diagram provided in Fig. S6.1 (Supplementary Information, SI). In brief, an image of the field diaphragm placed in the excitation beam path was formed at the sample plane (conjugate planes FD and SP, Fig. 6.1), while the excitation beam was homogenized and collimated (owing to the conjugate planes LS and BFP, Fig. 6.1). In order to reduce laser speckle induced sample illumination non-uniformity, the laser-coupling fibre was mechanically dithered at a frequency > 5 KHz. A zero-aperture adjustable iris diaphragm served as the field diaphragm allowing tailoring of the field-of-view at the sample plane, to a diameter as small as 20 μm that contained only several UCNP. The sample image was captured by an electron-multiplying CCD (EMCCD) camera (Andor iXon DU-885) mounted to the microscope detection port. An acousto-optic tuneable filter (AOTF) (LSi-300 Hyperspectral Imaging System, Gooch and Housego) was integrated into the detection path of the epi-luminescence microscope for hyperspectral imaging. The employed spectral range was 500 - 700 nm with 3-nm increments and a bandwidth of 3.7 nm. The spectral filter module (filter cube) contained a high-pass absorbance filter (cut-off 850 nm, Thorlabs) placed in the excitation beam path to remove the 978-nm laser side lobes. A dichroic beam-splitter (cut-off, 511 nm, Semrock) reflected the excitation light toward the sample, while passing the emitted light to the detection path. Two additional short-pass filters (cut-off, 842 nm, Semrock and cut-off, 700 nm, Thorlabs) in the detection channel suppressed the excitation light leakage (see Fig. S6.2, SI). At the sample plane, the TEM finder grid with deposited UCNP was placed on a microscope glass slide and covered with a standard cover slip.

6.2.3 Emission spectra (ensemble)

The UCNP powder was placed in a custom-designed sample holder that consisted of a thin glass plate (thickness, 0.45 mm) with a 1.5-mm diameter circular hole in the centre sandwiched between two glass cover-slips. The excitation fibre was butted against the UCNP powder glass facing the hole filled with the UCNP powder. The emission spectrum was measured in transmission using a calibrated fibre-coupled diffraction-grating based spectrometer (Ocean Optics) in conjunction with a short-pass emission filter (cut-off, 842 nm).

6.2.4 Conversion efficiency

Absolute conversion efficiency of ensemble UCNP

The UCNP powder was placed in the custom-designed sample holder (see section 6.2.3) at one of the exit ports of a 4-inch integrating sphere (Labsphere), as described by Page et al [15]. At the backside of the sample holder, a tilted aluminium-coated glass slide was placed to reflect the light back into the integrating sphere avoiding a double-pass through the sample. A multimode optical illumination fibre (fibre core 400 μm , NA 0.22) was butted against the sample holder at the centre of the hole. This assured precise control and reproducibility of the excitation spot size at the UCNP sample to calculate I_{ex} . Luminescence emitted by the UCNP sample was spatially integrated in the sphere by means

of multiple reflections from the walls, and eventually detected using a photodiode (PD) (Thorlabs, PDA-55) at the exit port positioned at 90° with respect to the illumination path. The signal from the PD was connected to a lock-in amplifier (Stanford Research Systems, model SR830) and the excitation laser (LD980-01CW CXCH-Photonics) that was pulsed (pulse generator, Stanford research systems, model DG535), with pulse width of 4 ms and frequency 125 Hz to enable reliable registration of the UCNP luminescence signals as low as $1 \mu\text{W}$. The I_{ex} range was controlled by the laser diode current and neutral density filters. The UCNP emission and unabsorbed excitation power were measured by inserting a short-pass (cut-off, 842 nm) and long-pass (cut-off, 830 nm, Semrock) filter, respectively, in the detection channel (in front of the PD). The performance of the interference filters and the detector channel collection efficiency was increased by positioning a high-power lens in the detection channel. The spectral response of the integrating sphere and PD was calibrated for a broad spectral range (470 – 1050 nm). By definition, η_{uc} was calculated as $P_{\text{em}}/P_{\text{abs}}$ [W/W]. P_{em} was determined by measuring the luminescence signal corrected for the absolute spectral response of the system and the UCNP spectral emission (see SI, Fig. S6.3a). P_{abs} was determined by measuring the excitation powers unabsorbed by a reference sample (TiO_2), P_{ref} and the UCNP powder, P_{UCNP} , so that $P_{\text{abs}} = P_{\text{ref}} - P_{\text{UCNP}}$. P_{abs} mainly resulted from the linear absorption of Yb^{3+} -ions. For robust estimation of P_{abs} the measurements were repeated for several excitation intensities and a linear fit was performed to calculate the absorbed fraction of the excitation light ($r^2 > 0.99$).

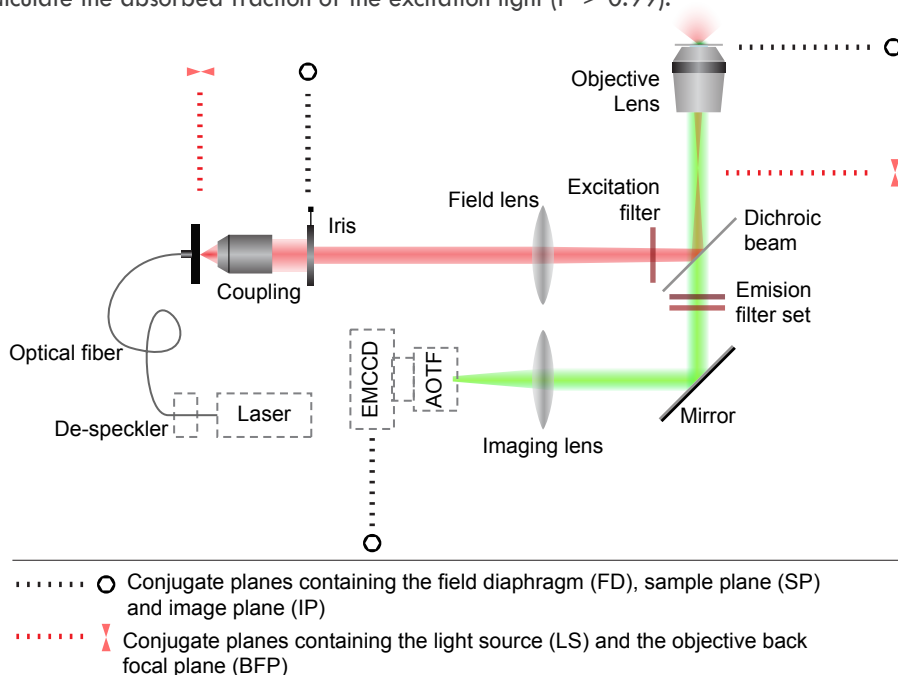


Figure 6.1 | Diagram of the custom-modified epi-luminescence imaging system employed for single-UCNP and spectral imaging. A wide-field inverted epi-luminescence microscope was modified to allow external fibre-coupled laser illumination. The optical fibre was dithered to average out speckles. The excitation light was configured to uniformly illuminate the field-of-view at the sample plane via a modified Köhler illumination scheme. The sample plane was imaged using an EMCCD camera, optionally mounted with an AOTF for hyperspectral imaging. An adjustable iris diaphragm allowed reduction of the field-of-view to restrict imaging to several single UCNP particles and small clusters.

Absolute conversion efficiency of single-UCNP

UCNPs sparsely deposited on the TEM finder grid were imaged using the epi-luminescence microscope set-up, as described earlier. The emitted power was determined by reading out the pixel values of the EMCCD image using the camera settings, sensitivity specifications and by calibrating the throughput of the microscope optics from sample plane to image plane. Two aspects of the EMCCD related to the epi-luminescence imaging are important to note: 1. The sensor quantum efficiency, $QE_{CCD}(\lambda)$ [number e^- / number photons] is wavelength-dependent, so that integration over the relevant wavelength range (400 - 800 nm) was necessary. 2. The camera electron-multiplication gain (EM gain) allowed straightforward multiplication of the pixel read-out values by the EM gain (in virtue of RealGame™ EMCCD feature). The UCNP signal read out by the sensor, S_{UCNP} , depended on the UCNP sample emitted intensity and the spectral calibration coefficient of the imaging system according to:

$$S_{UCNP} = N_{Yb} \sigma_{abs}^{Yb} I_{ex} \eta_{uc} \zeta_{total} + N_{el} \quad (6.1)$$

where S_{UCNP} and N_{el} [counts/s] are the signal per UCNP node and electronic noise level, respectively; N_{Yb} the number of Ytterbium (Yb^{3+}) ions per node that absorbed the excitation light; σ_{abs} [cm^2] the Yb^{3+} absorption cross-section (neglecting the absorption due to ~ 10 -fold fewer Er^{3+} ions and $\sigma_{Er,abs'} \ll \sigma_{Yb,abs'}$) [15, 26]; and ζ_{total} [counts/W/s] the calibration coefficient integrated over the UCNP emission spectrum (see Fig. S6.4). S_{UCNP} was the sum of the pixels that sampled an image of the UCNP node. The noise contained shot, dark and read noise components. Optical background was negligible (see Fig. S6.2). The number of Yb^{3+} per UCNP node was estimated using the $NaYF_4$ crystal lattice constants ($a = 5.991 \text{ \AA}$, $c = 3.526 \text{ \AA}$) [27], TEM-derived dimensions and numbers, and Na to Yb molar ratio [28]. ζ_{total} was calculated as:

$$\zeta_{total} = \int_{\lambda=400}^{\lambda=800} QE_{CCD}(\lambda) \zeta_{optics}(\lambda) N_{ph}(\lambda) d\lambda \frac{EMgain}{S_{CCD}} \quad (6.2)$$

where ζ_{optics} is the throughput of the imaging optics, N_{ph} the photon emission rate per wavelength per UCNP emission power [number of photons/W/s], $EMgain$ is a linear factor and S_{CCD} is the camera sensitivity [number of e^- /count]. The values of QE_{CCD} and S_{CCD} were provided by the EMCCD manufacturer. The absolute throughput ζ_{optics} was spectrally calibrated by imaging an optical fibre in the sample plane and comparing the known fibre output power to the power detected by the camera at the relevant wavelength range (see Fig. S6.5). In Fig. S6.4 the spectral output and the detector response are shown for UCNP imaging using a water- and blood-immersion objective.

6.3 RESULTS AND DISCUSSION

Realization of the prime goal of ultrahigh-sensitivity imaging of UCNPs in biological tissue is critically dependent on the attainable UCNP contrast, which is defined as the ratio of the detected luminescence signal (S) originating from the UCNPs to the background signal (B)

stemming from the residual biological tissue autofluorescence and noise. The signal estimation calls for a thorough characterization of the excitation and emission properties of UC-NPs, as well as quantification of the excitation/detection paths of the optical microscopy system adapted for ultrahigh-sensitivity imaging, where the adverse effects of the biological tissue on UCNP excitation and detection are taken into account. These effects are greatly exacerbated in the case of most fluorescent organic dyes, as will be shown in our cross-comparison study of optical imaging of a UCNP and fluorescein dye molecule in biological tissue. For the background signal estimation, the tissue optical properties (including scattering, absorption and autofluorescence) need to be considered. We commence by reporting on the measurement of absolute conversion efficiency and emission spectra of UCNPs, using an integrating sphere set-up and calibrated optical microscopy system (Section 6.3.1; ensemble and single-particle measurements). In Section 6.3.2 the quantitative assessment of single-UCNP imaging contrast in biological environment is addressed experimentally and theoretically, using haemolysed blood and skin models, respectively. We combine the physical characteristics of UCNPs, the optical properties of biological tissue and the abilities of advanced imaging systems to provide clear guidance towards intelligent development and a realistic application scope of upconversion nanomaterials.

6.3.1 Quantitative Characterization

Conversion Efficiency. Comments on Conventions

Conversion efficiency, η_{uc} , of UCNPs represents the most important parameter that governs the luminescence properties. It is defined as the emitted power/absorbed power (P_{em}/P_{abs}) expressed in W/W [15]. We note that this important parameter is used inconsistently across the literature. Traditionally, the term “quantum yield” (QY) is defined as the ratio of the number of photons emitted to the number of photons absorbed by the sample [29]. However, during the upconversion process one photon is emitted as a result of the absorption of two or more photons, thus the QY would not exceed 50% following this definition. In order to re-normalize this value, the QY of 2- or 3- photon absorption processes is scaled by a factor 2 or 3 respectively [16, 30], although not consistently in literature [13, 31]. In addition, the emission is the result of a complex, unknown combination of 2- and 3-photon excitation pathways [32, 33], rendering this approach speculative. For these reasons, the term “conversion efficiency” is believed to more adequately represent the net output of the complex upconversion process.

It is worthwhile to comment here on two other issues with UCNP conventions. Firstly, the dependency of η_{uc} on I_{ex} complicates the comparison of η_{uc} or QY measurements taken at different values of I_{ex} . For example, the reported QY values of 0.18% [22] and 0.47% [13] measured at $I_{ex} \sim 10^3$ W/cm² and 17.5 W/cm² respectively, are hardly comparable due to an unknown functional dependence of η_{uc} on I_{ex} . Secondly, quantitative reports on the absolute η_{uc} or related values are still scarce in literature [15, 31] often replaced by the limited-accuracy comparisons of UCNP emission with that of bulk phosphors or organic dyes [6, 23]. In order to address this lacuna, we present the results of the measurements of absolute η_{uc} of UCNPs synthesized in-house for a large range of excitation intensities up to I_{sat} .

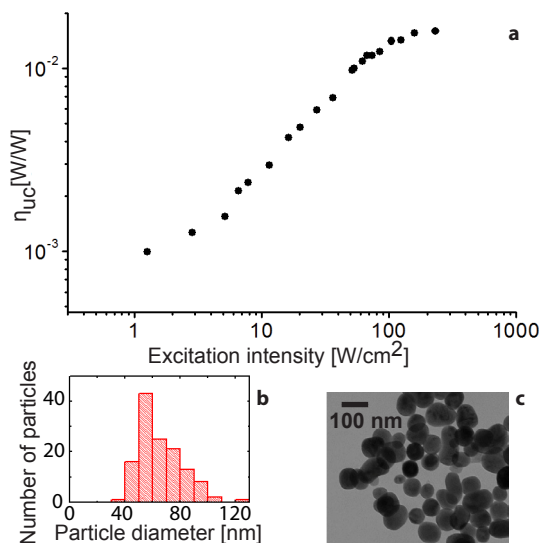


Figure 6.2 | Photophysical properties of UCNPs. (a) Plot of the absolute conversion efficiency (η_{uc}) [W/W] of the reported upconversion nanoparticle sample versus the excitation intensity at $\lambda_{ex} = 978$ nm measured using a calibrated integrating sphere set-up. η_{uc} is the ratio of the emitted power integrated over the entire emission spectral range (500-700 nm) to the absorbed power. (b) Size histogram obtained by analyzing the transmission electron microscopy (TEM) images of NaYF₄:Yb,Er UCNPs (330 particles) synthesized in-house. A typical TEM-image is shown in (c).

Photophysical Properties of As-Synthesized Upconversion Nanoparticles

We carried out characterization of the key photophysical properties of as-synthesized UCNPs in powder form. The β -NaYF₄ nanocrystals were synthesized following the thermal decomposition method, and co-doped with Yb³⁺ and Er³⁺ ions (β -NaYF₄:Yb,Er) at the most efficient molar ratio of 20% Yb³⁺ and 2% Er³⁺ [5, 28, 32]. The measurement of η_{uc} versus excitation intensity at the excitation wavelength (λ_{ex}) of 978 nm, was performed using a custom-modified integrating sphere set up. The integrating sphere ensured absolute measurement of the absorption and emission characteristics of UCNP powder independent of scattering by the sample. Size, morphology and η_{uc} results are summarized in Fig. 6.2 and full scale TEM images of variable magnification are provided in SI, Fig. S6.6. The synthesis yielded quasi-spherical UCNPs of diameters measured to be 68 ± 16 nm. The η_{uc} was measured to reach nearly 2% at $I_{ex} \equiv I_{sat} \cong 150$ W/cm², a high value in comparison with that of the comparably sized β -NaYF₄:Yb,Er sample reported by Boyer et al. [31], ($QY \approx 0.3\%$ at comparable I_{ex} , recalculated using the emission spectrum and photon energies to $\eta_{uc} \approx 0.5\%$), although the sample environment (organic solvent hexane known to quench η_{uc}) might account for this difference. As was expected for the supralinear upconversion process, the η_{uc} dropped dramatically at low I_{ex} , as can be seen in Fig. 6.2a. The UCNP emission spectra versus I_{ex} were acquired using a calibrated spectrometer and presented in Supplementary Information Fig. S6.3. These spectra exhibited two characteristic emission bands grouped in green (510-560 nm) and red (640-680 nm) emission multiplets, as shown in Fig. S6.3a. The red and green emission bands were attributed to the Er atomic transitions induced by the sequential two and three photon energy absorption processes [10]. The complex multi-step excitation process of the UCNPs is nonlinear, as manifested by the supralinear dependence of the emitted luminescence power, P_{em} on I_{ex} : $P_{em} \sim I_{ex}^n$, where the power index n varies versus I_{ex} reaching $n = 1$ at $I_{ex} = I_{sat}$. At low I_{ex} , n would ideally take discrete values of 2 or 3, reflecting the 2 or 3- step excitation process. However, the measured n takes the values of 1.5 and 1.9 for the green and red emission bands

respectively (Fig. S6.3c), reflecting more complex processes of the linear decay, excited state absorption, energy transfer upconversion, cross-relaxation and quenching, and their interrelations in the different upconversion pathways [16, 28, 33-35]. It is beyond the scope of this paper to elucidate these mechanisms. However, it is important to account for the spectral and η_{uc} dependence on the excitation intensity in a quantitative analysis of the UCNP imaging *in vivo*.

The complexity of the upconversion excitation/emission process is confounded by ensemble averaging, where the surface-related (non-radiative relaxation) processes can be concealed by inter-particle interactions. Characterization of an isolated individual UCNP is instrumental to remove this uncertainty.

Single Particle Spectral Imaging

A single upconversion nanoparticle represents an excellent measurement entity for the quantitative measurements of the emission spectra and η_{uc} , because it is unaffected by inter-particle interactions and has known physical dimensions. In order to establish this single-UCNP experimental model, we modified a wide-field epi-luminescence inverted microscope to allow uniform illumination of the sample plane with an external excitation laser (978 nm). A high-sensitivity EMCCD camera was incorporated in the microscope detection path. This imaging modality has several advantages, including short acquisition times (~ 1 s) at moderate $I_{ex} \cong 250$ W/cm² uniformly distributed across the field-of-view, as compared to scanning configurations that operate at $I_{ex} \cong 10^6$ W/cm² and with a pixel dwell time of 10 ms [22, 24], resulting in acquisition times of 40 minutes for a 512×512 pixel image. In order to demonstrate single-UCNP imaging, the as-synthesized powder was dispersed in organic solvent and sparsely deposited on a TEM grid pre-coated with a Formav© monolayer film. This enabled TEM and epi-luminescence imaging of the same sample areas to be matched and individual nanoparticles singled out. An example of this correlative imaging method is shown in Fig. 6.3, where the two top panels display the matched constellation of UCNPs acquired by TEM and epi-luminescence microscopy, respectively, and a single particle (designated “single”) is observable.

The utility of this single-UCNP imaging system is demonstrated by comparison of the luminescence spectra of single, clustered, and powder UCNP samples that were obtained using an acousto-optic tuneable filter (AOTF) integrated into the detection path of the epi-luminescence microscope. This enabled acquisition of spectral data from every pixel, converting our microscope into a hyperspectral imaging modality. The spectral responses of “single” and “cluster 2” were examined individually and locally by reading out spectral data from the corresponding pixels (Figures 6.4a and 6.3b). The emission spectra of the other small clusters were similar (data not shown). The ensemble-averaged spectrum of the UCNP powder was also obtained using the hyperspectral imaging mode (Fig. 6.4c) by processing a full-field image of the powder sample. In order to cross-validate the spectral measurements, the UCNP powder emission spectra were additionally acquired with a diffraction-grating based calibrated spectrometer (dashed curves, Fig. 6.4). The dependency of the spectral features on excitation intensity is discussed in Section 6.3.1 and Fig. S6.3. The spectral emissions of the individual, clustered and ensemble UCNPs showed a high resemblance at equivalent I_{ex} . Hence, the UCNP spectral luminescence profile appeared to

be primarily dependent on I_{ex} and independent on the inter-particle interactions in air, thus clarifying the speculations made by Wu et al. [24] This enabled accurate characterization of η_{uc} of single UCNPs, as described next.

Measurement of Single Particle Conversion Efficiency

Each node of the UCNP constellation shown in Fig. 6.3 can be characterized in terms of the number/dimension of nanoparticles per node and corresponding photon detection rate (encoded in false colour in Fig. 6.3b) that can be converted to photon emission rate (P_{em}) per excitation intensity, which suffices to determine the UCNP conversion efficiency, $\eta_{uc} = P_{em}/P_{abs}$. The photon emission rate integrated over the node was obtained by reading out and converting the corresponding image pixels, since the epi-luminescence detection channel throughput, and the EMCCD spectral quantum efficiency versus the camera settings were calibrated (see Eqs. 6.1 and 6.2, Figs. S6.5 and S6.4, SI). The conversion efficiency was found by:

$$\eta_{uc} = \frac{P_{em}}{P_{abs}} = \frac{(S_{UCNP} - N_{el}) / \zeta_{total}}{N_{YB} \sigma_{abs} I_{ex}} \quad (6.3)$$

where the quantities are explained in section 6.2.4.

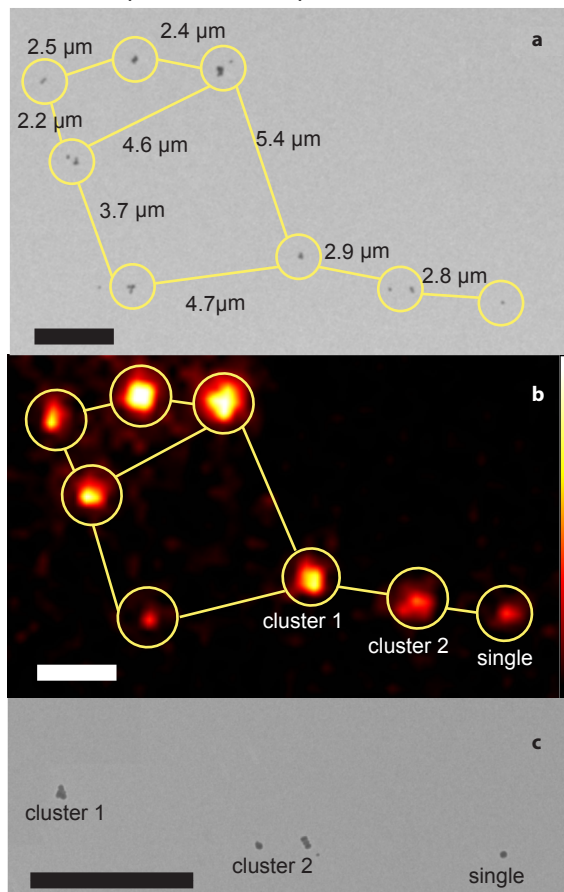


Figure 6.3. Single-UCNP correlative imaging using (a) TEM and (b) epi-luminescence microscopy images corresponding to the same areas of the sample TEM grid. The distances between the individual (encircled) nanoparticles/clusters, given in (a), were precisely matched to these in (b) to identify the same UCNP constellation. (c) Close-up TEM image of the same area as in (a), where UCNP sites designated ‘cluster 1’, ‘cluster 2’, and ‘single’ correspond to the three sites in (b). The individual UCNPs within ‘cluster 1’ and ‘cluster 2’ were optically unresolvable. ‘Single’ designates a single UCNP particle clearly observable, as a diffraction-limited spot in (b). The excitation wavelength, intensity and exposure time were 978 nm, ~ 250 W/cm² and 0.7 s, respectively. The pixel values were converted to photons/second (ph/s) and color-coded using the look-up color bar in (b).

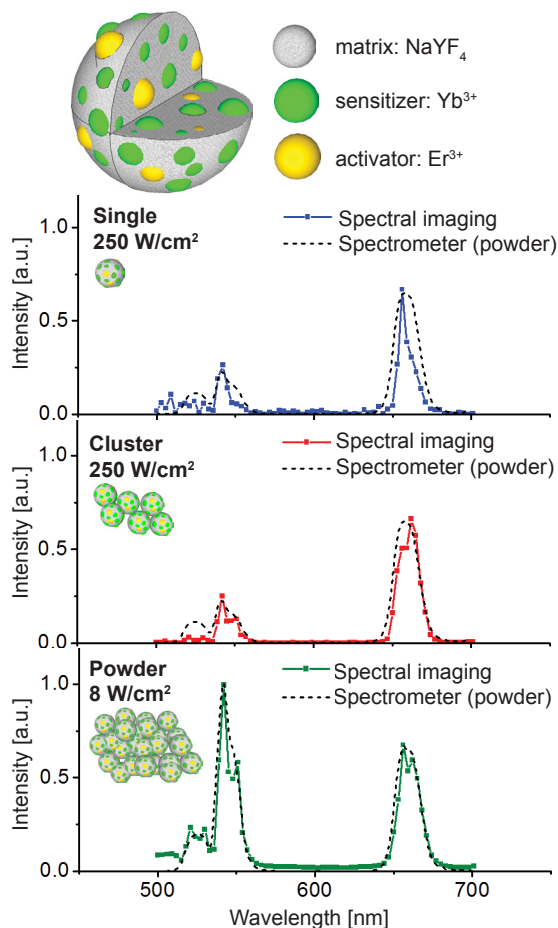


Figure 6.4 | Spectral imaging of UCNPs. Emission spectra of UCNPs in (a) single, (b) small cluster (designated ‘cluster 2’ in Figure 6.3) and (c) powder form (data points joined by solid lines) captured using hyperspectral epi-luminescence microscopy, overlaid with the ensemble-averaged spectra of UCNP powder captured by a calibrated spectrometer (dashed lines). The corresponding exposure times and EMCCD camera electron-multiplication (EM) gains were (a) 4 sec and 255; (b) 1.5 sec and 44; and (c) 0.014 sec and 9. Since the samples (a) and (b) contained considerably less emitters than the powder sample (c), the excitation intensities at $\lambda_{\text{ex}} = 978$ nm were varied, respectively, from 250 W/cm² to 8 W/cm² to accommodate for the large disparity in the emission signals that would otherwise exceed the dynamic range of the EMCCD. The decreased I_{ex} resulted in an increased green-to-red emission ratio in (c) due to the varied upconversion energy redistribution between the green and red multiplets. Top panel, schematic diagram of NaYF₄:Yb,Er UCNPs.

The calculated η_{uc} of the single UCNP and two clusters (as identified in Fig. 6.3) obtained by processing the image data is presented in Table 6.1 along with the relevant parameters. The excitation intensity corresponded to the saturation regime where the ensemble-averaged η_{uc} measured with the integrating sphere was nearly 2%. The calculated values of η_{uc} of the individual UCNP constellation nodes ranged between 1.2 and 2.0%, due to the variability in the host crystal composition and impurities. The independent η_{uc} measurements for the isolated and ensemble UCNPs exhibited excellent agreement, which indicates that the η_{uc} dependence on I_{ex} and emission peak ratios hold for single UCNPs. Although the absolute η_{uc} of the single-UCNP was marginally lower than that of the ensemble-averaged UCNPs, it was adequately high to enable ultrasensitive imaging at the single-particle sensitivity level in biological scenarios, as addressed in the following section.

6.3.2 Biomedical Imaging Applications

Single Particle Imaging Through Haemolysed Blood

The feasibility of single-UCNP imaging in a biological environment was explored by obscuring the UCNP sample with a highly absorbing biological fluid, such as blood, with re-

sults presented in Fig. 6.5. Whole blood (1 ml) was haemolysed by replacing plasma with distilled water. After centrifuging the supernatant was used to replace the water between the objective and sample plane to create a “blood-immersion objective”, as shown in Fig. 6.5a. The blood layer thickness was $\sim 250 \mu\text{m}$. Haemoglobin, the oxygen-carrying protein in red blood cells, is the main absorber in blood and has a distinct absorption spectrum, as shown in Fig. 6.5b. The UCNP emission spectrum is superimposed on the blood absorption spectrum to emphasize the high absorption in the green emission band and low absorption in the red emission band. This differential absorption by the blood altered the sample coloration, as shown in Fig. 6.5c. A low-magnification image of the UCNP sample illuminated by the 978-nm laser was captured by a digital colour camera through the eyepiece port of the epi-luminescence microscope, which reproduced the colour perception by the human eye. The UCNP sample appeared green (Fig. 6.5c, top panel), when using the standard water-immersion configuration of the objective lens, despite the prominent red band in the UCNP emission spectrum. This is explained by the higher spectral sensitivity of the eye to green colour compared to that of red colour (~ 20 times [36]). In case of the haemolysed “blood-immersion objective”, however (Fig. 6.5c, bottom panel), the green emitted light was largely absorbed by the haemoglobin, and the UCNP sample appeared red to the human eye and in the digital colour image. Hence, the UCNP red emission and NIR excitation passed with small losses through the biological fluid, suggesting the feasibility of imaging single UCNPs. This ultrahigh-sensitivity imaging through an obscuring biological fluid was demonstrated, as shown in Fig. 6.5d, where the previously identified single UCNP was clearly observable. Single-UCNP imaging has been reported using scanning [22, 24] and wide-field [23, 25] set ups, for exposed particles. To the best of our knowledge, this is the first demonstration of single-UCNP imaging in a biological medium, using a moderate excitation intensity ($250 \text{ W}/\text{cm}^2$) approaching the laser safety limits in a biological sample of realistic thickness. The demonstrated imaging through a $250\text{-}\mu\text{m}$ thick haemolysed blood layer is, for example, favourably comparable with the diameters of blood vessels in the microcirculation, which can be found in proximity to organ surfaces [37].

These experimental results show the feasibility of optical imaging of single upconversion nanoparticles in biological fluids, in accordance with the assessment of the photophysical properties. These results constitute an experimental platform from which the detection limits of single-particle imaging in live skin is assessed theoretically, as presented in the next section.

Table 6.1. Determination of the absolute η_{uc} using data from the calibrated epi-luminescence imaging of single and small clusters of UCNPs.

	P_{em} [W] (25%)	N_{yb} (10%)	$\sigma_{yb,obs}$ [cm^2] ^{b)}	I_{ex} [W/cm^2] (10%)	η_{uc} [%]
Cluster 1 ^{a)}	2.6×10^{-14}	5.5×10^5	1.0×10^{-20}	2.6×10^2	2.0 ± 0.5
Cluster 2 ^{a)}	2.2×10^{-14}	6.1×10^5	1.0×10^{-20}	2.6×10^2	1.3 ± 0.3
Single ^{a)}	4.9×10^{-15}	2.3×10^5	1.0×10^{-20}	2.6×10^2	1.2 ± 0.3

^{a)}As identified in Figures 6.3b and 6.3c. ^{b)}The Yb^{3+} absorption cross-section, as in Refs [14, 34]. Unites are given in square brackets, percentage standard deviations are given in brackets, except for η_{uc} .

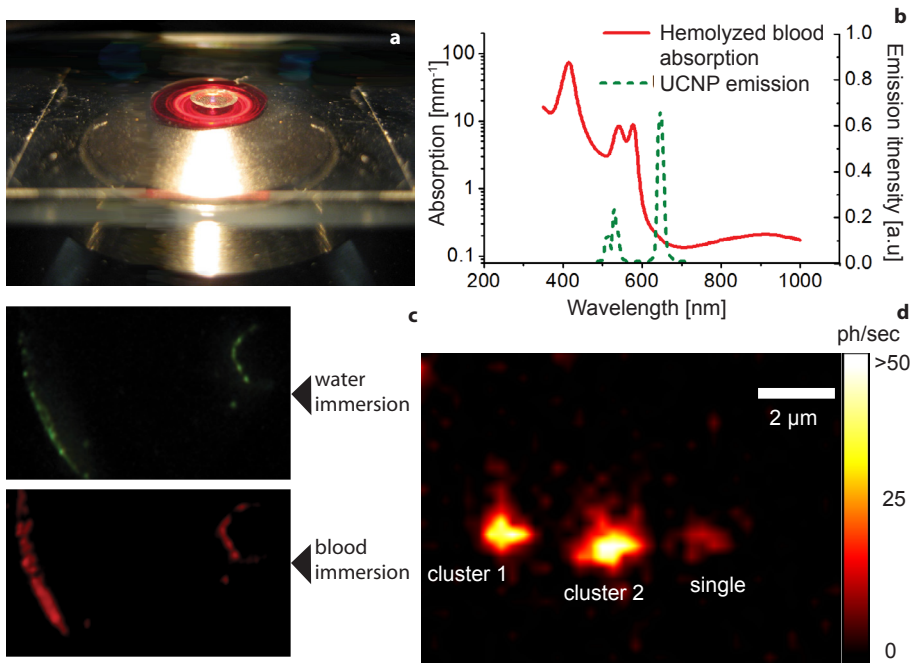


Figure 6.5 | Epi-luminescence imaging of a single UCNP using the “blood-immersion” objective. (a) A photograph of the haemolysed blood layer between the objective and cover slip. (b) Absorption spectrum of the haemolysed blood (red solid curve) and UCNP emission spectrum (green dashed curve). (c) Low-magnification images of the UCNP sample recorded through the eyepiece port using the water- (top) and blood- (bottom) immersion objective. The dried UCNP colloid rims appeared green (top) and red (bottom) due to the green light absorption by blood. (d) Epi-luminescence microscopy image of the UCNP constellation identified in Fig. 6.2c, imaged using the blood-immersion objective. The single UCNP is clearly observable, although blurred. The EMCCD camera settings and excitation parameters were equivalent to these of Fig. 6.2. The pixel values were converted to photons/second (ph/s) and colour-coded using the look-up bar in (d).

Modelling of Single Particle Imaging in Skin

In comparison with conventional *in vivo* fluorescence-assisted imaging, UCNP-assisted imaging offers the advantage of reduced excitation/emission light losses and complete suppression of the optical background due to tissue autofluorescence [11]. The implication of this improvement is demonstrated by a simplified quantitative comparison of imaging in skin using fluorescein (FL) and UCNPs at the single-particle level. The choice for this representative visible organic fluorescent dye is dictated by its broad acceptance in the field of experimental skin research *in vivo* in animals and humans [38], as well as in diagnostic procedures in skin [39] and other organs [40]. In our model, a single emitter (FL and UCNP) is considered buried in skin at a depth z . The calculated single-emitter signal (S) and background (B) values were compared in terms of their contrast (S/B) at different z . A confocal imaging setting is assumed in this model to reduce the adverse obscuring effect of out-of-focus signals that burden fluorescence-assisted imaging. The confocal imaging is known to improve the signal discrimination, such that the signals primarily originated from the focal volume at z .

The excitation power, $P_{0,ex}$ at the focal volume is attenuated according to Beer-Lambert's law: $P_{ex}(z) = P_{0,ex} e^{-\mu_{tr}z}$, where μ_{tr} is the transport attenuation coefficient [mm^{-1}] defined as a sum of the absorption, μ_a and reduced scattering coefficient, $\mu_s' = (1-g)\mu_s$, μ_s being the scattering coefficient, and g – the anisotropy factor. The attenuation is due to photon removal from the focusing path by absorption (μ_a) and isotropic scattering (μ_s'). μ_{tr} was computed in the visible and NIR spectral range using the reported values of μ_a and μ_s' for fresh Caucasian adult skin samples *in vitro*; while assuming a layered skin structure of epidermis, dermis and subcutaneous fat of corresponding thicknesses 80 μm , 400 μm and 520 μm , respectively [41]. The emitted power was calculated using $P_{em,UCNP} = N_{Yb} \sigma_{Yb,abs} I_{ex} \eta_{uc}$ and $P_{em,FL} = 1 \cdot \sigma_{FL,abs} I_{ex} \Phi_{FL}$ where I_{ex} – the excitation intensity at depth z calculated by dividing $P_{ex}(z)$ by the excitation area. Φ_{FL} – the FL conversion efficiency was taken as 0.9 and $\sigma_{FL,abs} = 3.5 \times 10^{-16} \text{ cm}^2$ at $\lambda_{ex} = 500 \text{ nm}$, [7] and 1 signifies a single FL emitter. $N_{Yb} \approx 1.1 \cdot 10^5$ was calculated using the NaYF_4 crystal lattice constants [27] and Na to Yb molar ratio [28] for a 70 nm particle, η_{uc} was obtained using the data plotted in Fig. 6.2a at the corresponding values of I_{ex} , and with $\sigma_{Yb,abs}$ as listed in Table 6.1. The maximum permissible exposure (MPE) for skin is tabulated as 200 W/cm^2 at 500 nm (FL) and 700 W/cm^2 at 978 nm (UCNP) for a 1-ms exposure time [42]. The UCNP emission is attenuated along the return path through skin, which was accounted for using μ_{tr} of skin at the UCNP and FL emission wavelengths. The isotropic emission collection efficiency was determined by the objective lens acceptance angle ($\text{NA} = 0.8$). The collected emission photo conversion by the EMCCD camera (moderate EM gain, $\times 100$) was computed using the calibration protocol presented earlier (Eqs. 6.1 - 6.3).

The single-UCNP imaging contrast was estimated using the background level set by the electronic noise, with dark and read noise components specified by the camera manufacturer (Andor), and shot noise calculated as $\sqrt{N_e}$ - (N_e - the photoelectron number before the EM-gain). The total noise was multiplied by the EM-characteristic multiplicative noise factor $\sqrt{2}$ [43]. The FL imaging background (B), however, had an additional autofluorescence-induced component. At $\lambda_{ex} = 500 \text{ nm}$, the autofluorescence was mainly due to the abundant endogenous fluorophore in skin, flavin adenine dinucleotide (FAD), whose concentration in skin was reported to be $\sim 1 \mu\text{g}/\text{mg}$ [44]. ~ 750 FAD molecules were situated in a $1\text{-}\mu\text{m}^3$ focal volume and contributed to B . In addition, the out-of-focus FAD-induced background signal was estimated following the model of confocal imaging by Magnor et al. for scattering media, assuming a homogeneous distribution of FAD in skin [45]. $\sigma_{FAD,abs}$ and Φ_{FAD} were taken as $6.0 \times 10^{-18} \text{ cm}^2$ at 500 nm and 0.033, respectively [46]. The FAD-induced electronic signal at the EMCCD camera was computed analogously to that of FL and UCNP, corrected for the spectral filtering of the FAD emission profile extending beyond the FL emission spectrum.

Fig. 6.6 shows a plot of the calculated imaging contrast of a single emitter versus depth in skin tissue. The absolute luminescence signal S from FL is high at the shallow imaging depths ($< 300 \mu\text{m}$) in comparison with that of UCNP, and so is B due to the autofluorescence by FAD (Fig. 6.6, inset). The resultant contrast provided by FL is therefore very modest, with the highest value of 2 at the skin surface. Taking into consideration the non-uniformity of autofluorescence across the skin sample, single-FL imaging is at best problematic, if at all possible, particularly given the serious issue of the short lifetime of FL before undergoing photobleaching. In regard to S/B of the single UCNP, the relatively low S was compensat-

ed by the extremely small B , almost invariable versus depth. The contrast is therefore, much higher, slowly decreasing from a value of 10 down to 3 over the 200- μm depth, which allows reliable detection of a single UCNP particle. Based on our model S/B reached a value of 1 at 400- μm depth in skin, however, due to a number of the simplifying assumptions made this is likely to be the best-case-scenario.

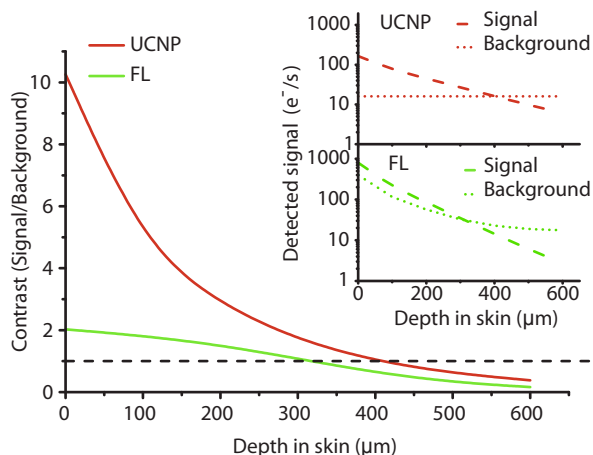


Figure 6.6 | Theoretical estimation of single-emitter detection sensitivity in skin. A plot of the optical (confocal) detection contrasts of a single upconversion nanoparticle (UCNP, brown) and organic fluorescence dye (fluorescein, FC, green) versus their depth in skin, as modelled theoretically. The inset shows more detailed quantitative plots of the imaging signal (dashed) and background (dotted) of UCNP and FL versus depth in skin expressed in electrons per second (e^-/s). The black dotted line demarcates the contrast value of 1. See text for details.

Feasibility of Single Particle Imaging in Biotissue

The remarkable progress in the synthesis of upconversion nanomaterials and demonstration of their unique luminescence properties have led to new possibilities in optical biomedical imaging using UCNPs. However, an uptake of this luminescent nanotechnology into cellular imaging is tempered by the existence of competitive luminescent nanomaterials that exhibit a high contrast against the dim autofluorescence background of cells (e.g. europium complexes, quantum dots). Nam et al. reported the imaging of UCNP-labelled live HeLa cells for 6 h using 980 nm excitation at $I_{\text{ex}} = 3 \text{ kW}/\text{cm}^2$, which allowed high-sensitivity intracellular imaging [47]. At these excitation intensities, *in vitro* single UCNP imaging in cells is feasible, as our results suggest. The scope of *in vivo* UCNP applications for optical deep tissue imaging of small lesions appears to be limited by the supralinear dependence of the upconversion luminescence on the excitation intensity, which is greatly diminished at $I_{\text{ex}} \ll I_{\text{sat}}$ in deep ($> 1 \text{ cm}$) tissue layers. This confines the application niche of UCNP-based molecular probes to optical luminescent imaging in biological fluids, subsurface tissue layers and thick biological tissue slices. Within these domains, the UCNP-based molecular probes exhibit outstanding performance and provide unparalleled imaging capabilities, as was demonstrated and modelled in this paper (Fig.'s 6.5 and 6.6). Such exceptional performance is achieved due to the unique photophysical properties of UCNP that allows evading the adverse effects of high absorption and autofluorescence of biological tissue, as long as the high excitation intensity is attainable by focusing.

The theoretical analysis highlights great promise for imaging single nanoparticles embedded in biological tissue, and provides a useful guidance to luminescent nanoparticle design (not necessarily limited to UCNPs) and optical imaging modality. For example, an improved photochemical design of UCNPs, e.g. co-doping NaYF_4 with Ytterbium and Thulium featuring an emission peak at 800 nm should further reduce the absorption by blood (Fig. 6.5) and result in an increased imaging depth [48]. A promising recent result was the synthesis of 42-nm UCNPs with an exceptional high conversion efficiency at 800 nm (3.5%) [49], using core-shell synthesis to reduce surface quenching [50]. The maximum imaging depth ($\text{SNR} > 1$) for the reported UCNP sample, with mean size 42 nm and the highest reported value of $\eta_{uc} = 3.5\%$, was found to be 450 μm (see SI, Fig. S6.7). There are several reports demonstrating UCNP-assisted imaging depths of 2 cm [13] and 3.2 cm [51] in live mice and fat tissue respectively. In this paper, the absolute detection sensitivity of single UCNP imaging *in vivo* is addressed, which can readily be extended to an ensemble of UCNPs.

At the same time, our presented optical imaging model was oversimplified. The confocal scanning modality is impractically slow due the long (sub-milliseconds) UCNP luminescence lifetime, which requires to the dwell time to be set to $\sim 500 \mu\text{s}$ per pixel to avoid smearing of the emission light onto adjacent pixels due to the UCNP after-glow [21]. On the other hand, the wide-field epi-luminescence modality suffers from the overshadowing of small single-UCNP signals by large UCNP clusters, so that on some occasions, we had to reduce the field diaphragm of the epi-luminescence microscope to collapse the field-of-view to a diameter of $\sim 20 \mu\text{m}$. The wide-field configuration was not efficient in suppressing out-of-focus signals, which precluded the use of whole blood due to scattering, and required blood haemolysis. This could possibly be prevented by optical clearing mechanisms that result in a reduced attenuation coefficient of whole blood [52]. Lastly, the NIR irradiation dose (250 W/cm^2 CW) still exceeded the maximum permissible exposure for skin. Although excitation at 980 nm at a ten-fold greater intensity has been shown to be tolerable to live cells for 6 h *in vitro* [47], continuous *in vivo* imaging at the excitation intensity as low as 0.5 W/cm^2 caused significant skin damage to mice [53], due to high water absorption in the live animal. Shifting the excitation wavelength from 980 to 915 nm was suggested to reduce water absorption. A pulsed laser excitation regime delivering high energy per pulse at a low repetition rate represents another possible solution to maintain acceptable imaging contrast within the laser safety limits. Therefore, advanced optical imaging – possibly, a hybrid of the wide-field epi-luminescence and confocal modalities – is required to harness the UCNP specificity and uniqueness.

There are a number of interesting prospects to employ UCNPs as molecular probes in tissues sites accessible to ballistic photons including skin, the superficial microcirculation and sub-surface lesions for luminescence-guided surgery. Recent reports demonstrate that imaging of low amounts of UCNP-labelled stem cells is feasible: as few as ~ 10 labelled cells were subcutaneously detected in nude mice and *in vivo* detection limits for UCNP-based imaging were an order of magnitude lower in comparison with QDs [54, 55]. UCNPs conjugated to a cancer-targeting peptide, for example somatostatin [56, 57] can facilitate the diagnosis of skin cancer [58]; detection of circulating tumour cells in subcutaneous blood vessels, or the sensitive guidance to tumour sites by receptor-targeted optical imaging [59]. Recently, we have successfully conjugated UCNPs with scFv4D5 mini-antibodies

raised against the human epidermal growth factor receptor (HER2/neu) overexpressed in e.g. breast adenocarcinoma cells and demonstrated high-specific binding *in vitro* (Chapter 7). Delivery of conjugated UCNP to tumours *in vivo* poses new challenges. The primary delivery mechanism of intravenous injected nanoparticles is thought to be the enhanced permeability and retention effect, caused by leaky blood vessel walls in tumour tissue. Subsequent nanoparticle diffusion into the tumour core occurs via intercellular or intracellular routes, where the latter mediated by endocytosis is more likely than the former due to the large nanoparticle size compared to the intercellular space [47, 60]. As a last example, UCNP-facilitated ion sensing by combining the optical properties of ion sensing chromophores/fluorophores with UCNP optical characteristics seems to be promising [61].

6.4. CONCLUSION

The adoption of upconversion nanomaterials in optical biomedical imaging demands specification of application areas where the UCNP merits are critical while the limitations are tolerable, and where the cutting-edge sensitivity required for UCNP-assisted imaging performance is achievable. We examined this ultrahigh-sensitivity optical imaging scenario by performing imaging and characterization of a single UCNP in a biological environment represented by haemolysed blood. In particular, the key UCNP parameters of absolute conversion efficiency and spectral emission were measured in individual and ensemble particles and found comparable. These experimental results were utilized in an idealized theoretical model, which was believed to aid identification of application areas of extreme sensitivity in challenging *in vivo* environments, including biological liquids, subsurface layers and thick tissue slices. Specifically, our theoretical skin imaging model showed that UCNP imaging had superior contrast over that of conventional fluorescent dyes. The background-free imaging of single upconversion nanoparticles at depths up to 400 μm in skin was found feasible. Therefore, the application scope of carefully tailored UCNP-based molecular probes is significant, including luminescence-guided surgery and ultrahigh-sensitivity bioassays in unprocessed biological fluids.

6.5 ACKNOWLEDGEMENTS

This work was performed in part at the OptoFab node of the Australian National Fabrication Facility, a company established under the National Collaborative Research Infrastructure Strategy to provide nano and microfabrication facilities for Australia's researchers.

6.6 REFERENCES

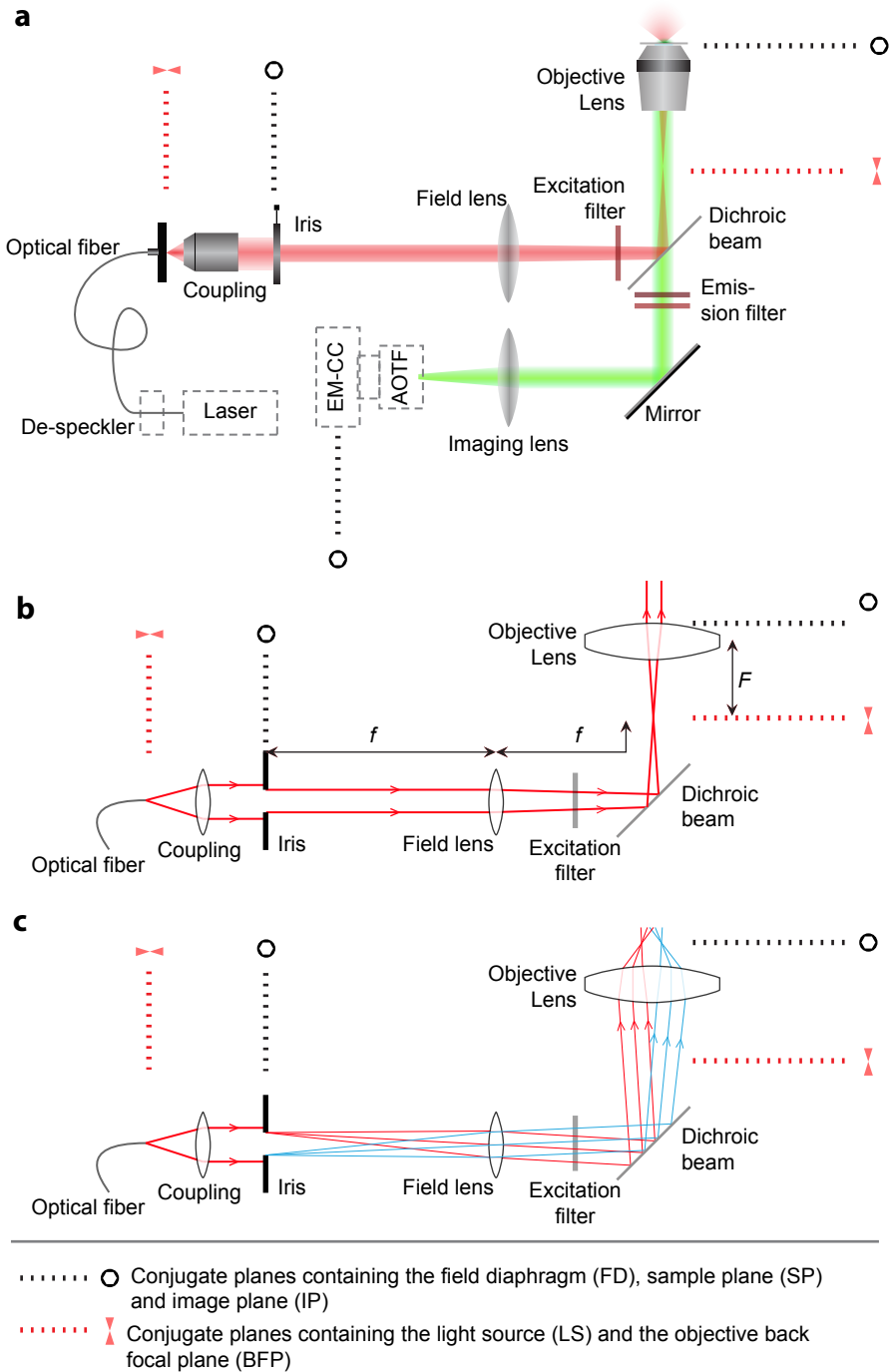
1. S. A. Hilderbrand and R. Weissleder, "Near-Infrared Fluorescence: Application to *In vivo* Molecular Imaging," *Curr. Opin. Chem. Biol.* 14, 9-71 (2009).
2. M. S. Patterson, B. Chance, and B. C. Wilson, "Time Resolved Reflectance and Transmittance for the Non-Invasive Measurement of Tissue Optical Properties," *Appl. Opt.* 28, 2331-2336 (1989).
3. A. Corlu, R. Choe, T. Durduran, M. A. Rosen, M. Schweiger, S. R. Arridge, M. D. Schnall, and A. G. Yodh, "Three-Dimensional *In vivo* Fluorescence Diffuse Optical Tomography of Breast Cancer in Humans," *Opt. Express* 15, 6696-6716 (2007).
4. B. E. Schaafsma, J. S. D. Mieog, M. Hutteman, J. R. van der Vorst, P. J. K. Kuppen, C. W. G. M. Löwik, J. V. Frangioni, C. J. H. van de Velde, and A. L. Vahrmeijer, "The clinical use of indocyanine green as a near-infrared fluorescent contrast agent for image-guided oncologic surgery," *J. Surg. Oncol.* 104, 323-332 (2011).
5. S. Heer, K. Kömpe, H. U. Güdel, and M. Haase, "Highly Efficient Multicolour Upconversion Emission in Transparent Colloids of Lanthanide-Doped NaYF₄ Nanocrystals," *Adv. Mater.* 16, 2102-2105 (2004).
6. G. Yi, H. Lu, S. Zhao, Y. Ge, W. Yang, D. Chen, and L. H. Guo, "Synthesis, Characterization, and Biological Application of Size-controlled Nanocrystalline NaYF₄: Yb, Er Infrared-to-Visible Up-Conversion Phosphors," *Nano Lett.* 4, 2191-2196 (2004).
7. U. Resch-Genger, M. Grabolle, S. Cavaliere-Jaricot, R. Nitschke, and T. Nann, "Quantum Dots Versus Organic Dyes as Fluorescent Labels," *Nat. Methods* 5, 763-775 (2008).
8. M. C. Mancini, B. A. Kairdolf, A. M. Smith, and S. Nie, "Oxidative Quenching and Degradation of Polymer-encapsulated Quantum Dots: New Insights Into the Long-Term Fate and Toxicity of Nanocrystals *In vivo*," *J. Am. Chem. Soc.* 130, 10836-10837 (2008).
9. K. Liu, X. Liu, Q. Zeng, Y. Zhang, L. Tu, T. Liu, X. Kong, Y. Wang, F. Cao, S. A. G. Lambrechts, M. C. G. Aalders, and H. Zhang, "Covalently Assembled NIR Nanoplatform for Simultaneous Fluorescence Imaging and Photodynamic Therapy of Cancer Cells," *ACS nano* 6, 4054-4062 (2012).
10. F. Auzel, "Upconversion and Anti-Stokes Processes With f and d Ions in Solids," *Chem. Rev.* 104, 139-174 (2004).
11. C. T. Xu, N. Svensson, J. Axelsson, P. Svenmarker, G. Somesfalean, G. Chen, H. Liang, H. Liu, Z. Zhang, and S. Andersson-Engels, "Autofluorescence Insensitive Imaging Using Upconverting Nanocrystals in Scattering Media," *Appl. Phys. Lett.* 93, 171103 (2008).
12. F. Leblond, S. C. Davis, P. A. Valdés, and B. W. Pogue, "Pre-Clinical Whole-Body Fluorescence Imaging: Review of Instruments, Methods and Applications," *J. Photochem. Photobiol.*, B. 98, 77-94 (2010).
13. Q. Liu, Y. Sun, T. Yang, W. Feng, C. Li, and F. Li, "Sub-10 nm Hexagonal Lanthanide-Doped NaLuF₄ Upconversion Nanocrystals for Sensitive Bioimaging *in vivo*," *J. Am. Chem. Soc.* 133, 17122-17125 (2011).
14. C. Vinegoni, D. Razansky, S. A. Hilderbrand, F. Shao, V. Ntziachristos, and R. Weissleder, "Transillumination Fluorescence Imaging in Mice Using Biocompatible Upconverting Nanoparticles," *Opt. Lett.* 34, 2566-2568 (2009).
15. R. H. Page, K. I. Schaffers, P. A. Waide, J. B. Tassano, S. A. Payne, W. F. Krupke, and W. K. Bischel, "Upconversion-pumped Luminescence Efficiency of Rare-Earth-doped Hosts Sensitized With Trivalent Ytterbium," *JOSA B* 15, 996-1008 (1998).
16. J. Suyver, A. Aebischer, D. Biner, P. Gerner, J. Grimm, S. Heer, K. Krämer, C. Reinhard, and H. Güdel, "Novel Materials Doped With Trivalent Lanthanides and Transition Metal Ions Showing Near-Infrared to Visible Photon Upconversion," *Opt. Mater.* 27, 1111-1130 (2005).
17. M. P. Hehlen, G. Frei, and H. U. Güdel, "Dynamics of infrared-to-visible upconversion in Cs₃Lu₂Br₉: 1% Er³⁺," *Phys. Rev. B* 50, 16264 (1994).
18. W. R. Zipfel, R. M. Williams, R. Christie, A. Y. Nikitin, B. T. Hyman, and W. W. Webb, "Live Tissue Intrinsic Emission Microscopy Using Multiphoton-excited Native Fluorescence and Second Harmonic Generation," *Proc. Natl. Acad. Sci. U. S. A.* 100, 7075 (2003).
19. F. Wang, J. Wang, and X. Liu, "Direct Evidence of a Surface Quenching Effect on Size-Dependent Luminescence of Upconversion Nanoparticles," *Angew. Chem. Int. Ed.* 122, 7618-7622 (2010).
20. T. Kelf, V. Sreenivasan, J. Sun, E. Kim, E. Goldys, and A. Zvyagin, "Non-Specific Cellular Uptake of Surface-Functionalized Quantum Dots," *Nanotechnology* 21, 285105 (2010).
21. J. Pichaandi, J. C. Boyer, K. R. Delaney, and F.

- C. J. M. van Veggel, "Two-Photon Upconversion Laser (Scanning and Wide Field) Microscopy using Ln³⁺-Doped NaYF₄ Upconverting Nanocrystals A Critical Evaluation of their Performance and Potential in Bio-imaging," *J. Phys. Chem. C.*, 19054–19064 (2011).
22. A. D. Ostrowski, E. M. Chan, D. J. Gargas, E. M. Katz, G. Han, P. J. Schuck, D. J. Milliron, and B. E. Cohen, "Controlled Synthesis and Single Particle Imaging of Bright, Sub-10 nm Lanthanide-Doped Upconverting Nanocrystals," *ACS nano* 6, 2686–2692 (2012).
 23. G. Mialon, S. Türkcan, G. Dantelle, D. P. Collins, M. Hadjipanayi, R. A. Taylor, T. Gacoin, A. Alexandrou, and J. P. Boilot, "High Up-Conversion Efficiency of YVO₄: Yb, Er Nanoparticles in Water Down to the Single-Particle Level," *J. Phys. Chem. C.*, 22449–22454 (2010).
 24. S. Wu, G. Han, D. J. Milliron, S. Aloni, V. Altoe, D. V. Talapin, B. E. Cohen, and P. J. Schuck, "Non-blinking and Photostable Upconverted Luminescence from Single Lanthanide-Doped Nanocrystals," *Proc. Natl. Acad. Sci. U. S. A.* 106, 10917–10921 (2009).
 25. Y. I. Park, J. H. Kim, K. T. Lee, K. S. Jeon, H. B. Na, J. H. Yu, H. M. Kim, N. Lee, S. H. Choi, and S. I. Baik, "Nonblinking and nonbleaching up-converting nanoparticles as an optical imaging nanoprobe and T1 magnetic resonance imaging contrast agent," *Adv. Mater.* 21, 4467–4471 (2009).
 26. G. Lakshminarayana, J. Ruan, and J. Qiu, "NIR Luminescence From Er-Yb, Bi-Yb and Bi-Nd Codoped Germanate Glasses for Optical Amplification," *J. Alloys Compd.* 476, 878, (2009).
 27. H. X. Mai, Y. W. Zhang, R. Si, Z. G. Yan, L. Sun, L. P. You, and C. H. Yan, "High-Quality sodium rare-earth fluoride nanocrystals: controlled synthesis and optical properties," *J. Am. Chem. Soc.* 128, 6426–6436 (2006).
 28. K. W. Krämer, D. Biner, G. Frei, H. U. Güdel, M. P. Hehlen, and S. R. Lüethi, "Hexagonal Sodium Yttrium Fluoride Based Green and Blue Emitting Upconversion Phosphors," *Chem. Mater.* 16, 1244–1251 (2004).
 29. W. Melhuish and M. Zander, "Nomenclature, Symbols, Units and Their Usage in Spectrochemical Analysis-VII. Molecular Absorption Spectroscopy, Ultraviolet and Visible (UV/VIS) " *Pure Appl. Chem* 56, 231–245 (1984).
 30. V. Tikhomirov, G. Adamo, A. Nikolaenko, V. Rodriguez, P. Gredin, M. Mortier, N. Zheludev, and V. Moshchalkov, "Cathodo- and photoluminescence in Yb³⁺ Er³⁺ Co-Doped PbF₂ Nanoparticles," *Opt. Express* 18, 8836–8846 (2010).
 31. J. C. Boyer and F. C. J. M. Van Veggel, "Absolute Quantum Yield Measurements of Colloidal NaYF₄: Er³⁺, Yb³⁺ Upconverting Nanoparticles," *Nanoscale* 2, 1417–1419 (2010).
 32. H. X. Mai, Y. W. Zhang, L. D. Sun, and C. H. Yan, "Highly Efficient Multicolor Up-conversion Emissions and Their Mechanisms of Monodisperse NaYF₄: Yb, Er Core and Core/Shell-Structured Nanocrystals," *J. Phys. Chem. C.* 111, 13721–13729 (2007).
 33. Y. Wang, L. Tu, J. Zhao, Y. Sun, X. Kong, and H. Zhang, "Upconversion Luminescence of β -NaYF₄: Yb³⁺, Er³⁺@ β -NaYF₄ Core/Shell Nanoparticles: Excitation Power Density and Surface Dependence," *J. Phys. Chem. C.* 113, 7164–7169 (2009).
 34. M. Pollnau, D. Gamelin, S. Lüthi, H. Güdel, and M. Hehlen, "Power Dependence of Upconversion Luminescence in Lanthanide and Transition-Metal-Ion Systems," *Phys. Rev. B.* 61, 3337 (2000).
 35. J. Shan, M. Uddi, R. Wei, N. Yao, and Y. Ju, "The Hidden Effects of Particle Shape and Criteria for Evaluating the Upconversion Luminescence of the Lanthanide Doped Nanophosphors," *J. Phys. Chem. C.* 114, 2452–2461 (2010).
 36. Commission Internationale de l'Eclairage Proceedings, Commission Internationale de l'Eclairage Proceedings (Cambridge University Press, Cambridge, United Kingdom, 1931).
 37. E. C. Boerma, K. Mathura, P. van der Voort, P. Spronk, and C. Ince, "Quantifying Bedside-derived Imaging of Microcirculatory Abnormalities in Septic Patients: A Prospective Validation Study," *Crit. Care* 9, R601–R606 (2005).
 38. A. Bollinger, J. Frey, K. Jäger, J. Furrer, J. Seglias, and W. Siegenthaler, "Patterns of Diffusion Through Skin Capillaries in Patients With Long-Term Diabetes," *N. Engl. J. Med.* 307, 1305–1310 (1982).
 39. S. Dietherle, J. Lademann, H. J. Röwert-Huber, E. Stockfleth, C. Antoniou, W. Sterry, and S. Astner, "In-Vivo Diagnosis and Non-Invasive Monitoring of Imiquimod 5% Cream for Non-Melanoma Skin Cancer Using Confocal Laser Scanning Microscopy," *Laser Phys. Lett.* 5, 752–759 (2008).
 40. P. L. Hsiung, J. Hardy, S. Friedland, R. Soetikno, C. B. Du, A. P. Wu, P. Sahbaie, J. M. Crawford, A. W. Lowe, and C. H. Contag, "Detection of colonic dysplasia in vivo using a targeted heptapeptide and confocal microendoscopy," *Nat. Med.* 14, 454–458 (2008).
 41. E. Salomatina, B. Jiang, J. Novak, and A. N.

- Yaroslavsky, "Optical properties of normal and cancerous human skin in the visible and near-infrared spectral range," *J. Biomed. Opt.* 11, 064026 (2006).
42. Standards Australia Limited/Standards New Zealand, AS/NZS 60825 (SAI Global Limited, Sydney, AU and Wellington, NZ, 2012), 1-48.
 43. M. S. Robbins and B. J. Hadwen, "The noise performance of electron multiplying charge-coupled devices," *IEEE Transactions on Electronic Devices* 50, 1227-1232 (2003).
 44. O. A. Bessey, O. H. Lowry, and R. H. Love, "The Fluorimetric Measurement of the Nucleotides or Riboflavin and Their Concentration in Tissues," *J. Biol. Chem.* 180, 755-769 (1949).
 45. M. Magnor, P. Dorn, and W. Rudolph, "Simulation of confocal microscopy through scattering media with and without time gating," *JOSA B* 18, 1695-1700 (2001).
 46. S. D. M. Islam, T. Susdorf, A. Penzkofer, and P. Hegemann, "Fluorescence quenching of flavin adenine dinucleotide in aqueous solution by pH dependent isomerisation and photo-induced electron transfer," *Chem. Phys.* 295, 137-149 (2003).
 47. S. H. Nam, Y. M. Bae, Y. I. Park, J. H. Kim, H. M. Kim, J. S. Choi, K. T. Lee, T. Hyeon, and Y. D. Suh, "Long-Term Real-Time Tracking of Lanthanide Ion Doped Upconverting Nanoparticles in Living Cells," *Angew. Chem.* 123, 6217-6221 (2011).
 48. N. Dong, M. Pedroni, F. Piccinelli, G. Conti, A. Sbarbati, J. R. Hernandez, L. M. Maestro, M. C. Iglesias de la Cruz, F. Sanz-Rodriguez, and A. Juarranz, "NIR-to-NIR Two-Photon Excited CaF₂: Tm³⁺, Yb³⁺ Nanoparticles: Multifunctional Nanoprobes for Highly Penetrating Fluorescence Bio-Imaging," *ACS nano* 5, 8665-8671 (2011).
 49. C. T. Xu, P. Svenmarker, H. Liu, X. Wu, M. E. Messing, L. R. Wallenberg, and S. Andersson-Engels, "High-Resolution Fluorescence Diffuse Optical Tomography Developed with Nonlinear Upconverting Nanoparticles," *ACS nano* (2012).
 50. G. S. Yi and G. M. Chow, "Water-soluble NaYF₄: Yb, Er (Tm)/NaYF₄/polymer core/shell/shell nanoparticles with significant enhancement of upconversion fluorescence," *Chem. Mater.* 19, 341-343 (2007).
 51. G. Chen, J. Shen, T. Y. Ohulchanskyy, N. J. Patel, A. Kutikov, Z. Li, J. Song, R. K. Pandey, H. Ågren, and P. N. Prasad, "(α -NaYbF₄: Tm³⁺)/CaF₂ Core/Shell Nanoparticles with Efficient Near-Infrared to Near-Infrared Upconversion for High-Contrast Deep Tissue Bioimaging," *ACS nano*, 8280-8287 (2012).
 52. V. V. Tuchin, X. Xu, and R. K. Wang, "Dynamic optical coherence tomography in studies of optical clearing, sedimentation, and aggregation of immersed blood," *Appl. Opt.* 41, 258-271 (2002).
 53. Q. Zhan, J. Qian, H. Liang, G. Somesfalean, D. Wang, S. He, Z. Zhang, and S. Andersson-Engels, "Using 915-nm Laser Excited Tm³⁺/Er³⁺/Ho³⁺ Doped NaYbF₄ Upconversion Nanoparticles for *In vitro* and Deeper *In vivo* Bioimaging Without Overheating Irradiation," *ACS nano*, 3744-3757 (2011).
 54. C. Wang, L. Cheng, H. Xu, and Z. Liu, "Towards whole-body imaging at the single cell level using ultra-sensitive stem cell labeling with oligo-arginine modified upconversion nanoparticles," *Biomaterials* (2012).
 55. L. Cheng, K. Yang, S. Zhang, M. Shao, S. Lee, and Z. Liu, "Highly-sensitive multiplexed *in vivo* imaging using PEGylated upconversion nanoparticles," *Nano Res* 3, 722-732 (2010).
 56. V. K. A. Sreenivasan, E. J. Kim, A. K. Goodchild, M. Connor, and A. V. Zvyagin, "Targeting somatostatin receptors using *in situ*-bioconjugated fluorescent nanoparticles," *Nanomedicine* (2012).
 57. V. K. A. Sreenivasan, O. A. Stremovskiy, T. A. Kelf, M. Heblinski, A. K. Goodchild, M. Connor, S. M. Deyev, and A. V. Zvyagin, "Pharmacological Characterization of a Recombinant, Fluorescent Somatostatin Receptor Agonist," *Bioconjugate Chem.* 22, 1768-1775 (2011).
 58. B. D. Nguyen and A. E. McCullough, "Imaging of Merkel Cell Carcinoma 1," *Radiographics* 22, 367-376 (2002).
 59. A. Becker, C. Hennesius, K. Licha, B. Ebert, U. Sukowski, W. Semmler, B. Wiedenmann, and C. Grözinger, "Receptor-targeted Optical Imaging of Tumors With Near-Infrared Fluorescent Ligands," *Nat. Biotechnol.* 19, 327-331 (2001).
 60. H. R. Kim, K. Andrieux, S. Gil, M. Taverna, H. Chacun, D. Desmaële, F. Taran, D. Georgin, and P. Couvreur, "Translocation of poly (ethylene glycol-co-hexadecyl) cyanoacrylate nanoparticles into rat brain endothelial cells: role of apolipoproteins in receptor-mediated endocytosis," *Biomacromolecules* 8, 793-799 (2007).
 61. L. Xie, Y. Qin, and H.-Y. Chen, "Direct Fluorescent Measurement of Blood Potassium with Polymeric Optical Sensors Based on Upconverting Nanomaterials," *Anal. Chem.* (2013).

Figure S6.1 | Set-up and Köhler ray diagram. The set-up consisted of a wide-field inverted epi-fluorescence microscope (Olympus IX70) equipped with a water-immersion objective (40x, NA 1.15, Olympus). The laser illumination was guided to the sample plane using a modified illumination path replacing the default Mercury/Xenon arc lamp housing. To achieve homogeneous illumination at the sample plane and to have precise control over the field-of-view, a modified Köhler illumination scheme was built as is shown in panel (a). The two Köhler illumination ray diagrams illustrating the homogeneous illumination light ray path and the image forming light ray path are shown in panels (b) and (c) respectively. The conjugate planes are explained in the legend. In (b) a collimated laser beam filled the adjustable iris located at the back focal plane of the field lens, which was, in turn, one focal distance away from the back focal plane of the objective resulting in even and collimated sample illumination. In (c) the image forming function of the Köhler scheme is depicted: the image of the iris located at the focal point of the field lens resulted in the formation of its image at the objective focal plane. The magnification of the iris image was the ratio between the focal lengths of the objective and the field lens (~28x in this setup). A zero-aperture iris was used to control the illumination area. The other components of the set-up are an electron-multiplying CCD (EMCCD) camera (Andor iXon DU-885) and an acousto-optic tunable filter (AOTF) (LSi-300 Hyperspectral Imaging System, Gooch and Housego) mounted to the left side port of the microscope; excitation and emission filters; a 978 nm laser (LD980-01CW, CXCH-Photonics) and a mechanical dither to average out speckles. These components are further discussed in the main paper.

SUPPLEMENTARY INFORMATION



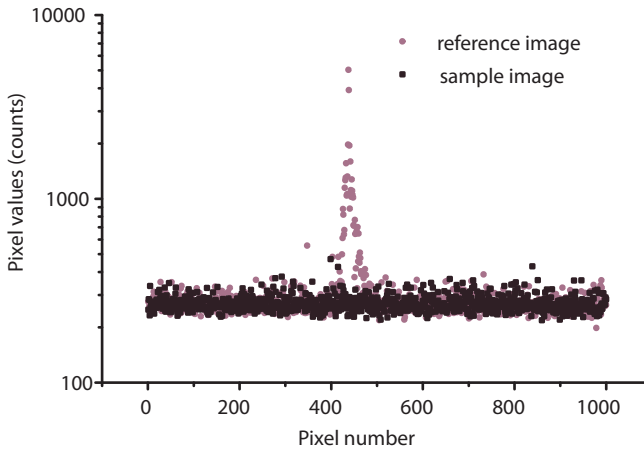


Figure S6.2 | Reference and sample image intensity. To estimate the amount of excitation light bleeding through the emission filter set and reaching the EMCCD camera, we imaged a TEM-grid with reference material (TiO_2) and obtained the pixel values on a line through the field-of-view on the image. The graph shows the pixel values in counts for each pixel along the line (pixel number) for the reference TEM-grid and for a TEM-grid with UCNP sample deposited. As can be seen no elevation of pixel value was observed for the reference image at the field-of-view, whereas the sample image pixel values increased at the focus spot due to detection of upconverted light. The detected signal was nonzero due to addition of a pixel base level and (low) values for read and dark noise. We can conclude that virtually no excitation light reached the detector.

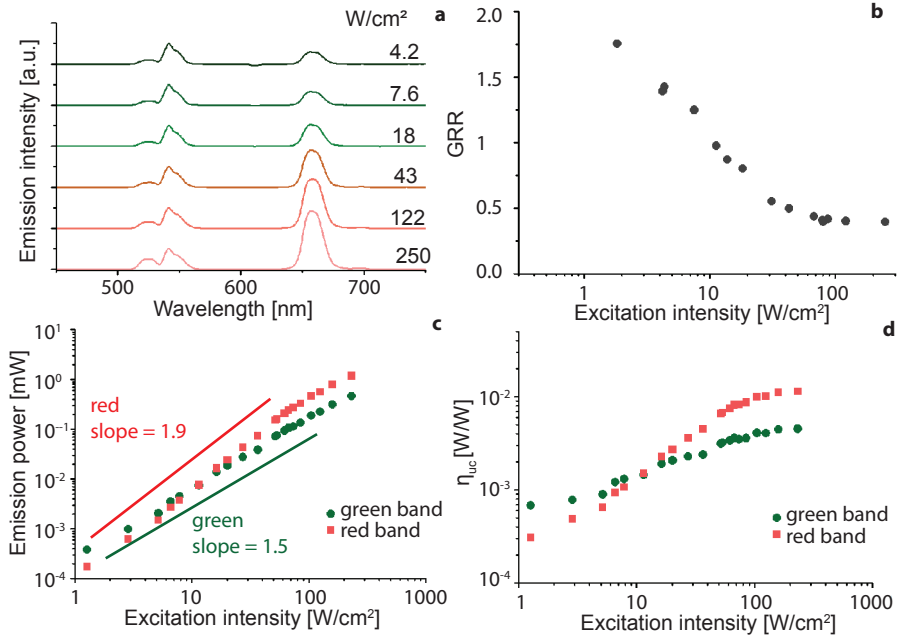


Figure S6.3 | Excitation intensity dependence of the green and red emission bands. (a) Ensemble emission spectra of UCNP powder were measured in transmission using a customized glass sample holder and calibrated spectrometer for several excitation intensities at excitation wavelength 978 nm (see section 6.2.3). The spectra were normalized at the 540 nm peak and are presented with an offset for clarity. (b) Integrating the spectra of (a) over the green and red emission band resulted in a green-to-red-ratio (GRR) dependence on excitation intensity. In (c), the emitted power dependence on excitation intensity in the green and red emission band is plotted on a double-logarithmic scale that showed a linear slope until emission saturation is reached around 150 W/cm². The slope is 1.9 for red emission and 1.5 for green emission, confirming a nonlinear emission process that involves at least 2 photons. Panel (d) shows the conversion efficiency (η_{uc}) dependence of the green and the red emission bands on excitation intensity.

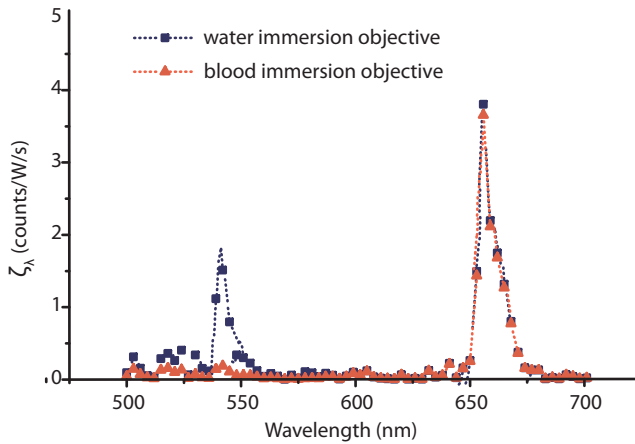


Figure S6.4 | Calibrated detector response for single UCNP immersed in water or blood. Using the emission spectrum of the single UCNP (Fig. 6.4a) and Eq. 6.2 the spectral calibration coefficient for each wavelength can be calculated using $EM_{gain} = 1$, $S_{ccd} = 0.89$ [e-/count], N_{ph} the number of photons per second per UCNP emission power of 1 W per wavelength [photons/W/s] and QE_{ccd} the detector quantum efficiency [e-/photon] per wavelength. Data points are connected by a dotted line as guide to the eye. In case of the haemolysed blood-immersion objective the signal is reduced due to absorption by haemoglobin. Integrating over all wavelengths (using spline interpolation) results in total counts/W/s for UCNP emission, referred to as ζ_{total} .

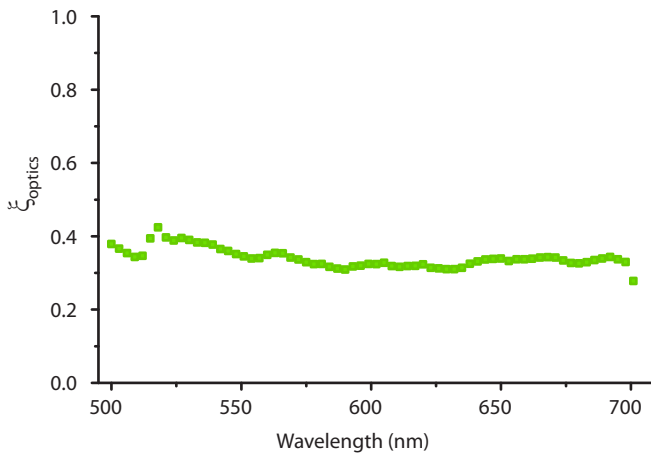


Figure S6.5 | Spectral throughput of inverted epi-luminescence microscopy system. The absolute throughput, ζ_{optics} , defined as $Signal_{sensor-plane} / Signal_{sample-plane}$ of the microscope imaging system was obtained by imaging an optical fibre (multimode, 100 μm core, NA 0.22) placed at the sample plane of the microscope. The output power of the fibre was measured using a calibrated power meter (Thorlabs). Using the camera settings and sensitivity specifications the power detected by the sensor can be calculated from the image pixel values, and subsequently the throughput can be obtained. This was done for several wavelengths and spectrally interpolated using a white light source (Ocean Optics LS-1, tungsten halogen), as plotted in the graph. The discontinuity around 510 nm was due to the dichroic beam splitter with a cut-off wavelength at 511 nm. Assuming isotropic emission of upconverted light by the UCNPs, the actual throughput of the system needed to be corrected for the acceptance angle of the microscope objective, a factor $1/3$ for NA = 1.15 (not shown).

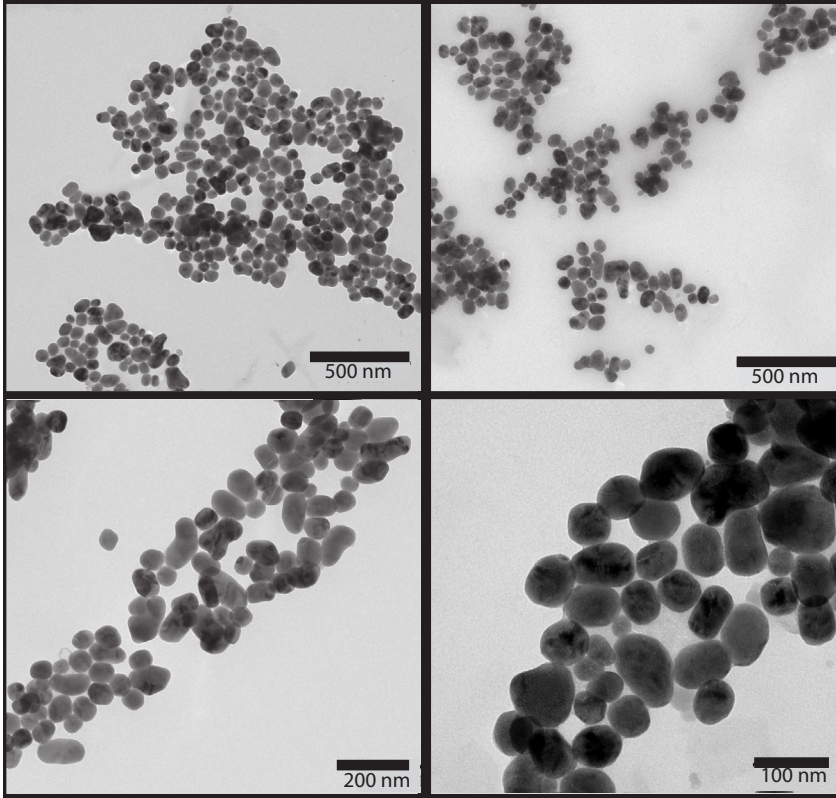


Figure S6.6 | TEM images with different magnifications of in-house synthesized UCNPs.

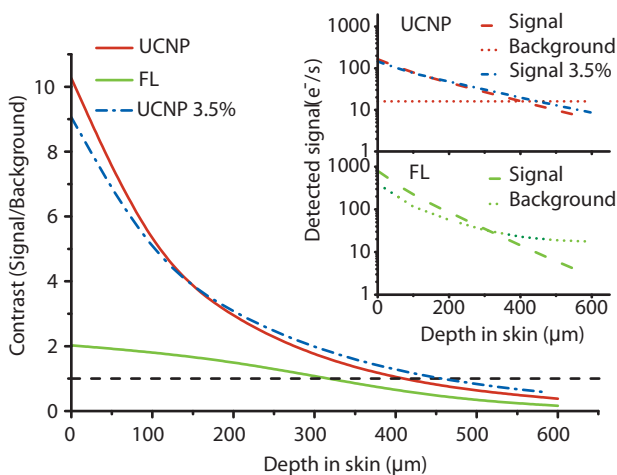


Figure S6.7. Theoretical estimation of single UCNP detection sensitivity in skin, a comparison between in-house synthesized and state-of-the-art UCNPs (Yb,Tm-co-doped core-shell UCNPs, ref 49), possessing the highest reported conversion efficiency 3.5%. Using our model described in Section 6.3.2, we calculated the imaging signal contrast and plotted the result (blue dot-dashed line) together with the previous results for fluorescein and the 70-nm UCNP. The 42-nm 3.5%-UCNP has a reduced absorption of excitation light due to the smaller size of the particle which reduced the imaging contrast, but the higher η_{uc} and the reduced transport attenuation coefficient of skin for the luminescence signal resulted in a higher contrast at increasing depth. The maximum imaging depth in skin is 450 μm , with contrast 1.